Materials Today Nano 21 (2023) 100298

Contents lists available at ScienceDirect

Materials Today Nano

journal homepage: https://www.evise.com/profile/#/MTNANO/login

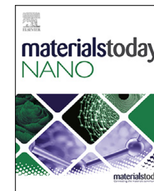

Revealing local order via high energy EELS

J.L. Hart [a, b, 1], A.C. Lang [b, c], Y. Li [d], S. Shahrezaei [e], D.D. Alix-Williams [a], M.L. Falk [a, f], S.N. Mathaudhu [e, g], A.I. Frenkel [d, h], M.L. Taheri [a, *]

[a] Department of Materials Science and Engineering, Johns Hopkins University, Baltimore, MD, USA
[b] Department of Materials Science and Engineering, Drexel University, Philadelphia, PA, USA
[c] American Society for Engineering Education Postdoctoral Fellowship, Washington, DC, USA
[d] Department of Materials Science and Chemical Engineering, Stony Brook University, Stony Brook, NY, USA
[e] Materials Science and Engineering Program, University of California, Riverside, CA, USA
[f] Department of Physics and Astronomy, Department of Mechanical Engineering, Hopkins Extreme Materials Institute, John Hopkins University, Baltimore, MD, USA
[g] Department of Mechanical Engineering, University of California, Riverside, CA, USA
[h] Division of Chemistry, Brookhaven National Laboratory, Upton, NY, USA

ARTICLE INFO

Article history:
Received 12 September 2022
Received in revised form
30 November 2022
Accepted 11 December 2022
Available online 20 December 2022

Keywords:
Short range order
Electron energy loss spectroscopy
Extended fine structure analysis
Bulk metallic glasses
Transmission electron microscopy

ABSTRACT

Short range order (SRO) is critical in determining the performance of many important engineering materials. However, accurate characterization of SRO with high spatial resolution − which is needed for the study of individual nanoparticles and at material defects and interfaces − is often experimentally inaccessible. Here, we locally quantify SRO via scanning transmission electron microscopy with extended energy loss fine structure analysis. Specifically, we use novel instrumentation to perform electron energy loss spectroscopy out to 12 keV, accessing energies which are conventionally only possible using a synchrotron. Our data is of sufficient energy resolution and signal-to-noise ratio to perform quantitative extended fine structure analysis, which allows determination of local coordination environments. To showcase this technique, we investigate a multicomponent metallic glass nanolaminate and locally quantify the SRO with <10 nm spatial resolution; this measurement would have been impossible with conventional synchrotron or electron microscopy methods. We discuss the nature of SRO within the metallic glass phase, as well as the wider applicability of our approach for determining processing−SRO−property relationships in complex materials.

© 2022 Elsevier Ltd. All rights reserved.

1. Introduction

The structure of materials with long-range crystalline order is completely described by a unit cell. Conversely, materials which lack long range periodicity can be described in terms of their short range order (SRO), here defined as the local atomic arrangements and compositional motifs within the first few nearest neighbor shells. In many emerging systems, SRO critically influences material properties and performance, *e.g.* the functional properties of nanoparticles [1,2], strain-hardening and shear band formation in bulk metallic glasses (BMGs) [3−5], surface passivation for materials in extreme environments [6], mechanical properties and radiation tolerance of high entropy alloys [7−11], dielectric response of relaxor ferroelectrics [12], and electrical performance of phase-change memory materials [13]. Conventionally, SRO is studied with total X-ray and neutron scattering, or X-ray absorption spectroscopy (XAS) with extended X-ray absorption fine structure (EXAFS) analysis [14,15]. However, these techniques average the local structure over very large areas defined by the beam size, either ignoring or incorrectly interpreting the effects of local heterogeneity. (Scanning) transmission electron microscopy ((S)TEM) offers Å-scale spatial resolution, but standard (S)TEM methods (*e.g.* imaging, diffraction, elemental mapping) cannot accurately determine SRO in complex, multi-element, and disordered systems. Hence, mapping SRO evolution across a sample's microstructure remains an experimental challenge. This shortcoming limits our understanding of how material processing influences SRO, and in turn, how SRO affects material properties. These issues must be addressed for SRO-based materials engineering and optimization.

* Corresponding author.
E-mail address: mtaheri4@jhu.edu (M.L. Taheri).
[1] present address: Department of Materials Science and Engineering, Cornell University, Ithaca, NY 14853, USA.

https://doi.org/10.1016/j.mtnano.2022.100298
2588-8420/© 2022 Elsevier Ltd. All rights reserved.

A promising strategy for local SRO quantification is to combine the benefits of STEM and X-ray synchrotron scattering within a single instrument − a vision described by L. M. Brown in his 1997 paper "A Synchrotron in a Microscope" [16]. Specifically, we consider STEM electron energy loss spectroscopy (EELS) with extended energy loss fine structure (EXELFS) analysis. Similar to the synchrotron EXAFS method, EXELFS analysis focuses on core-loss excitation spectra, from ~50 to 1000 eV past the edge onset. Data analysis allows the quantification of element-specific bond lengths, coordination numbers, and coordination species, providing a detailed understanding of SRO. Compared to synchrotron EXAFS, STEM-EXELFS offers a ~1000 fold increase in spatial resolution. However, extended edge analysis is ideally performed on high energy edges, usually >3 keV. While synchrotron XAS allows reliable measurement out to several 10s of keV, the EELS signal-to-noise ratio (SNR) and energy resolution both become limiting factors above 1 keV [17–23]. As such, prior EXELFS experiments have primarily focused on low energy edges [24–30], which hinders quantitative data analysis and prohibits the study of important edges, *e.g.* the *K*-edges of 3*d* transition metals or the *L*-edges of period 5 and 6 elements. In recent years, major steps have been taken solve this impasse. Craven et al. demonstrated the importance of the TEM/spectrometer optical coupling at high energy [18], and, using an optimized coupling, MacLaren et al. reported EELS measurements out to at a record 10 keV [19]. Still, the high energy EELS SNR and energy resolution remain too low for EXAFS-type data quantification, and mapping of SRO with STEM-EXELFS has only been performed at energies <1 keV [31,32].

In this article, we demonstrate the ability to locally quantify SRO with STEM-EXELFS of edges out to >10 keV, greatly increasing the number of accessible elements and the level of SRO quantification (Fig. 1). We maximize spectral quality using a direct detection sensor and an optical coupling optimized for high energy losses (Supplementary Fig. 1). With this experimental set-up, we are able to collect data out to 10+ keV with energy resolution and SNR comparable to that of a synchrotron. To demonstrate the new science enabled by this method, we perform localized Ni *K*-edge (8.3 keV) measurements in a nanolaminate of crystalline Ni and a Zr–Ni–Cu–Al BMG [40]. Through EXELFS analysis, we quantify the SRO in the BMG layer with ~7 nm spatial resolution, which would have been impossible to measure with XAS or conventional (S)TEM techniques. The ability to spatially map local bonding and coordination has far reaching implications for the study of complex and disordered materials.

2. Results

Our high energy EELS set-up has two primary components. First, we use a direct detection (DD) electron sensor, which allows counting of incident electrons. Relative to a traditional CCD camera, the DD sensor greatly increases the signal-to-noise ratio and the combined energy resolution and energy field of view. These advantages have proven critical for applications such as *in situ* and low dose EELS [33–39].

Secondly, we use a post-specimen lens configuration optimized for high energy losses. With inelastic electron scattering, the angular distribution follows a Lorentzian, with a characteristic angle θ_E that is proportional to the energy-loss [41]. Hence, for higher energy edges, electrons are scattered to higher angles, and a larger collection angle is preferred. Additionally, because the STEMs standard camera lengths are designed for the primary beam energy, it is necessary to ensure that high-loss electrons are also transferred to the spectrometer with an appropriate collection angle. As shown in Supplementary Fig. 1, our system is well-suited for high energy EELS; at 8 keV energy loss, the collection angle is 60 mrad, which is approximately $3 \times \theta_E$. One potential drawback to using large collection angles is that the collected spectra may include non-dipole contributions. However, as shown below, our EELS data is in excellent agreement with XAS reference data. This suggests that for our on-axis spectrometer, dipole scattering dominates any non-dipole contributions [41,42].

2.1. Benchmarking high energy EELS

First, we demonstrate the ability to measure high energy edges with high SNR using a focused electron probe. For these benchmarking experiments, we use a ~3 nm STEM probe of several nA. The probe was continuously scanned over a region of ~50×50 nm^2 during EELS collection, with acquisition times of 10–50 min (see section 4). Fig. 2 presents side-by-side comparisons of EELS and XAS measurements for several reference edges: the *K*-edge of Ti (5 keV), the *K*-edge of Ni (8.3 keV), and the L_3-edge of Au (11.9 keV) (see Supplementary Fig. 2 for EELS processing and normalization workflow). In general, agreement between the two techniques is excellent, indicating the high quality of our EELS data. Notably, the near edge EELS and XAS data are almost indistinguishable at the Ni *K*-edge.

At the Ti *K*-edge, the sharp pre-peak (marked with an *) acts as a resolution test for our EELS system (at this specific energy). Though there is some broadening relative to the XAS data, the pre-peak is clearly resolved in our EELS measurement. Based on the width of this feature, we estimate an EELS energy resolution better than 2 eV at 5 keV energy-loss ($\Delta E/E = 4 \times 10^{-4}$). We note that the Ti *K*-edge was previously studied with EELS by Blanche et al., and we highlight two key improvements in our data [17]. First, the energy resolution is improved by roughly a factor of 5, which is needed for quantitative fine structure analysis. Second, we have reduced the required electron dose by a factor of ~65, which is essential for local STEM analysis, as well as the study of beam sensitive materials. At the Au L_3-edge, agreement between the two techniques is somewhat worsened. This is likely due to the absence of sharp spectral features to use as a focusing metric. Still, our Au L_3-edge measurement captures the main features observed in the XAS data, and to our knowledge, this is the highest energy EELS result reported to date.

Next, we compare the EXELFS and EXAFS data. We follow the standard EXAFS procedure of isolating and normalizing the extended edge signal and then converting the excited (photo) electron energy to its wave number, obtaining $\chi(k)$ [43]. The EXELFS versus EXAFS comparisons are shown in Fig. 2 insets. Excellent agreement is evident, with clear $\chi(k)$ oscillations observed in the EXELFS data out to at least 10 Å^{-1} for all edges.

To further verify the quality of our data, we perform *ab initio*, multiple-scattering modeling of our EXELFS data using EXAFS analysis procedures [44]. Fig. 3a shows a fit to the Ni *K*-edge which includes the first 4 coordination shells of FCC Ni, and Fig. 3b shows a fit to the Au L_3-edge including the first two coordination shells of FCC Au (fitting of the Ti *K*-edge is shown in Supplementary Fig. 3). The data is displayed in *R*-space, where $\chi(R)$ is the Fourier transform of $\chi(k)$, and the modulus $|\chi(R)|$ is closely related to the radial distribution function of the excited atom. Each fit includes minimal free parameters: the amplitude reduction factor S_0^2, an energy offset ΔE, an isotropic lattice strain ε, and bond length mean square deviations σ^2 applied to the different coordination shells (section 4).

The excellent agreement between experiment and theory proves our ability to probe local atomic structure from core-loss edges out to 12 keV energy loss, all while using just a 3 nm STEM probe. Prior STEM-EXELFS studies have been limited to <1 keV energy loss [31,32], which greatly restricts the number of accessible elements. Additionally, the increased occurrence of absorption

edges at low energy confines the post-edge energy field-of-view, which in turn limits the quantification in R-space. Our analysis of the Ni K-edge includes a ~1 keV energy field of view (with a k-space fit window of $\Delta k = 11$ Å^{-1}), which gives an R-space bond-length resolution of $\Delta R = \pi/2\Delta k \sim 0.15$ Å. This level of EXELFS data quantification is unprecedented and was previously only possible with an X-ray beam.

2.2. STEM-EXELFS investigation of local order

To illustrate the novel science enabled by high energy STEM-EXELFS, we investigate an accumulative roll-bonded nano-laminate of a BMG ($Zr_{65}Cu_{17.5}Ni_{10}Al_{7.5}$) and crystalline Ni. Such composite structures of a BMG and crystalline metal show promise for improved mechanical performance and ductility, which is important for the commercial success of BMGs [45,46]. The accumulative roll-bonding process starts with ~mm thick sheets of crystalline Ni and the amorphous BMG stacked together. Through iterative rolling, cutting, and restacking of the rolled layers, the two sheets are fused together and the individual layer thicknesses approach the μm or nm scale [40]. The chosen BMG has a large supercooled liquid region, which is ideal for the roll-bonding process [40]. Prior studies have shown that roll-bonding can drive diffusion between layers and alter the constituent BMGs composition [47–51]. It is unclear, however, if there are also changes to the BMG's SRO, which is sensitively tied to mechanical properties [4,52]. Owing to the sub-micron width of the BMG layers, the local structure cannot be isolated from the Ni matrix using standard X-ray or neutron measurements (Fig. 4a). Conventional (S)TEM analysis of BMGs can determine the elementally-averaged radial distribution function, as well as structural and chemical order on length scales greater than a few nm [53–55]. But a complete understanding of BMGs – and multicomponent disordered solids in general – requires local EXAFS-type quantification of element-specific bonding, which cannot be obtained with existing methods.

In Fig. 4 we present localized EXELFS measurements from the nanoscale BMG phase. The sample geometry is shown in Fig. 4b. Note that with the imaging conditions used here, diffraction from crystalline phases leads to varying degrees of dark/light contrast; the uniform intensity of the BMG layer reflects its amorphous structure. The dashed box in Fig. 4b indicates the region of EELS analysis. First, we performed conventional EELS measurements of the Ni L-edge, Cu L-edge, and Zr L-edge. The evolution of these edges across the BMG layer is shown in Fig. 4c. In agreement with prior studies, we find that the Ni content within the BMG layer is much higher near the interface, suggesting inter-layer Ni diffusion. Next, we performed a high energy EELS spectrum image of the Ni K-edge. From the 2D spectrum image, we integrate the data parallel to the Ni/BMG interface, and then plot the data in R-space (Fig. 4d). The spectra in Fig. 4d are color-coded with the arrows in Fig. 4c to mark their spatial position. The extracted spectra have areal dimensions of 3×30 pixels^2, with a 2 nm pixel size and 3 nm STEM spot size. This corresponds to a ~7 nm spatial resolution normal to the Ni/BMG interface. Comparing the Ni K-edge $|\chi(R)|$ data from the BMG and the adjacent Ni matrix, the BMG shows a much weaker and broader first shell peak, indicative of a lower average coordination number and increased disorder. The peak position is also shifted to slightly lower R, which is attributed to anharmonicity in the bond distribution [56].

To quantify the local Ni bonding environment, we simplify our analysis of the Zr–Cu–Ni–Al system to a pseudo-binary Zr-(Ni,Cu) glass. This step is justified owing to i) the low concentration of Al, ii) the topological equivalence of Ni and Cu within this solution [57], and iii) the similar EXELFS signatures of Ni–Ni and Ni–Cu bonding (note that the local environment of Ni and Cu clusters can be independently analyzed through EXELFS measurements of the Ni and Cu K-edges, but for our analysis of the Ni K-edge, Ni–Ni and Ni–Cu bonds cannot be differentiated). With this simplification, we fit the first coordination shell of Ni using two bonds, Ni–Zr and Ni–Ni, the latter representing both Ni–Ni and Ni–Cu bonds. We fit each of the spatially resolved EXELFS spectra independently, allowing us to locally determine the Ni coordination environment (section 4).

To analyze chemical SRO within the BMG layer, we use the well-known Warren-Cowley parameter α [15,58,59],

$$\alpha_{Ni-Zr} = 1 - \frac{CN_{Ni-Zr}/CN_{Ni-Tot}}{X_{Zr}} \tag{1}$$

where CN_{Ni-Zr} is the number of Zr atoms within the first-shell of Ni, $CN_{Ni\text{-}Tot}$ is the total number of atoms in Ni's first shell, and X_{Zr} is the Zr atom fraction. The case of $\alpha \sim 0$ indicates no preferential bonding; $\alpha < 0$ indicates preferential bonding between Ni and Zr, i.e. anti-clustering or local ordering; and $\alpha > 0$ indicates clustering. BMGs generally show preferential solute-solvent bonding, and several EXAFS studies have found $\alpha < 0$ for bulk Zr–Ni–Cu glasses [60,61].

In Fig. 4e we present the SRO analysis. First we plot the ratio of $CN_{Ni-Zr}/CN_{Ni\text{-}Tot}$ as determined from our EXELFS fits. Across the entire width of the BMG layer, $CN_{Ni-Zr}/CN_{Ni\text{-}Tot} < 0.5$, indicating that Ni atoms are predominately coordinated with other Ni and Cu atoms. We also plot the local Zr atom fraction, X_{Zr}, as determined form our conventional EELS measurement. From these quantities, we then calculate $\alpha_{Ni\text{-}Zr}$ according to Eq. (1) (Fig. 4e). Across the entire BMG layer, α is positive, indicating a preference for Ni-(Ni,Cu) clustering. We emphasize that the local Ni structure could not have been directly obtained with EXAFS (owing to the X-ray beam size [62]) or conventional STEM techniques, which cannot directly probe local order in multi-component, disordered samples. We note that chemical SRO in BMGs can also be characterized by the Cargill equation [63], which accounts for differences in total coordination between species, *i.e.* differences in $CN_{Ni\text{-}Total}$ and $CN_{Zr\text{-}Total}$. However, because we cannot experimentally access $CN_{Zr\text{-}Total}$, we used the Warren-Cowley equation.

The finding of Ni-(Ni,Cu) clustering provides new insight into the complex thermomechanical processing of the composite. As noted above, bulk BMGs tend to show $\alpha < 0$ [4,57,64,65], which is in stark contrast to the clustering found here. The observed clustering is likely related to the extreme thermo-mechanical processing of the composite, which involves both significant strain and inter-layer diffusion. To understand how mechanical strain may influence SRO, we analyzed data from molecular dynamics simulations of $Cu_{64}Zr_{36}$ glasses as previously reported in Ref. [66]. Specifically, we compare the local structure in the as-quenched $Cu_{64}Zr_{36}$ glass versus highly deformed material at the center of a shear band (Supplementary Fig. 4). There is no evidence of increased clustering within the deformed material, suggesting strain is not the primary mechanism. Instead of deformation, the role of inter-layer Ni diffusion (which is enhanced due to deformation [47–49]) may be responsible for the observed SRO. We posit that Ni diffusing into the BMG concentrates in local Ni clusters, which leads to a positive value of $\alpha_{Ni\text{-}Zr}$.

We briefly comment on other results from the BMG fits, which are detailed in Supplementary Table 4. The best fit $R_{Ni\text{-}Ni}$ and $R_{Ni\text{-}Zr}$ are mostly constant across the BMG layer, and generally within 0.1 Å of the summed metallic radii for Ni–Ni and Ni–Zr, respectively. The total CN for Ni was rather low within the BMG, averaging just 6.8. The $CN_{Ni\text{-}Tot}$ within Zr–Ni–Cu BMGs is usually closer to 10 or 12 [67], though there are numerous EXAFS reports of $CN_{Ni\text{-}Tot} < 6$ for Zr-Ni [61] and other Ni containing BMGs [68,69]. We also note

that there is an inherent artifact for total CN determination when fitting EXELFS and EXAFS data for structures with strong, asymmetric bonding disorder [70–72]. Hence, the actual total CN may be higher than our fitted results, if the asymmetry in the unknown bonding distribution is taken into account.

3. Discussion and conclusions

Our EXELFS approach enables highly localized measurement of atomic structure and bonding, with a spot size three orders of magnitude smaller than those conventionally used with EXAFS. Moreover, EXELFS offers chemical specificity, as opposed to (S)TEM diffraction methods. This ability is relevant for the characterization of disordered, nanostructured and/or heterogeneous materials, for which local measurements of SRO were previously inaccessible. As a topical example, we studied nearest neighbor chemical order in a BMG, offering a snapshot of local clustering which could not have been revealed through conventional means. This demonstration is highly relevant to the long-standing challenge of accurate SRO characterization in BMGs [3–5,73–75]. We note a recent finding that compression of a similar Zr–Ni–Cu BMG altered the local order, which lead to work hardening and greatly improved mechanical behavior [3]. However, the specific nature of the altered SRO in Ref. [3] is unclear, further highlighting the importance of our methodology in closing this knowledge gap.

Another relevant material system for STEM-EXELFS analysis is high and medium entropy alloys. In these materials, the presence of SRO is hotly debated, as is the potential impact on material properties [7–9,76–79]. Recently, a (S)TEM imaging and diffraction study demonstrated the presence of medium range order in aged CoCrNi on the length scale of 3–4 nearest neighbor shells, and the observed order was linked to increased hardness [7]. However, questions remain over the presence of SRO within the 1st and 2nd nearest neighbor shells, which STEM-EXELFS is well positioned to answer. Our method is equally relevant for materials ranging from relaxor ferroelectrics, to electronic phase change materials, to functional nanoparticles. In all cases, the ability to locally quantify SRO will help establish processing–SRO–property relationships.

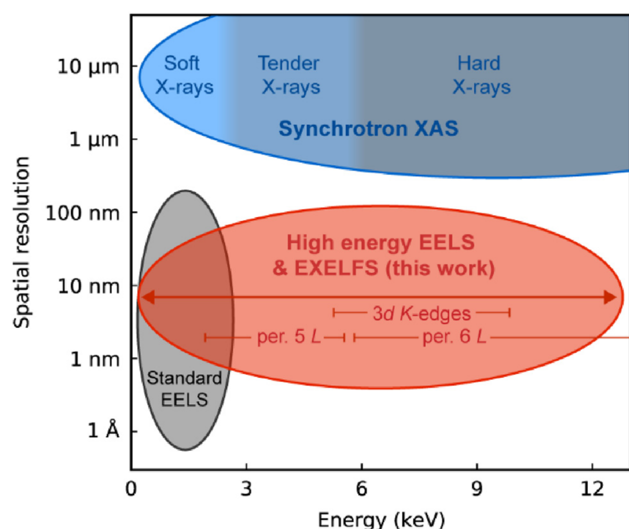

Fig. 1. Comparison of electron energy loss and X-ray absorption spectroscopies. Synchrotron XAS provides excellent SNR and energy range, but a limited spatial resolution. Conversely, standard EELS provides nanoscale spatial resolution, but limited SNR and energy range. The energy range of the 3*d* metal *K*-edges, and the period 5 and 6 *L*-edges are shown.

We demonstrated that EELS, as a single instrument, is capable of providing spectral analysis from ~1 eV out to >10 keV, spanning the soft to hard X-ray regimes (Fig. 1). This improved spectral range will enable efficient analysis of materials with both light and heavy elements [80]. For chemical analysis, the improved spectral range will facilitate efficient acquisition of multiple edges of a single element, *e.g.* the *L*- and *K*-edges of 3*d* transition metals, allowing more comprehensive chemical bonding analysis.

Lastly, we comment on some aspects of high energy EELS which require further improvement. While the SNR demonstrated here is sufficient for high energy EXELFS, the EELS energy resolution and calibration present a significant challenge above 10 keV, as apparent in our Au L_3-edge data (Fig. 2). Improved methods for spectrometer alignment and calibration are required for near edge fine structure analysis at these energies. Beam induced specimen damage presents an additional challenge, since large currents are necessary to obtain adequate SNR at high energy (in this study, the beam current ranged from 2 to 8 nA, see section 4). Here, the investigated Ti, Ni, and Au reference samples are heavy enough to avoid knock-on damage under the 200 keV beam. For the investigated BMG sample, there may be some level of knock-on damage [81], but the EXELFS signal showed no dose-dependence, indicating that the electron beam did not alter the chemical SRO (Supplementary Fig. 5). Conversely, many oxide, biological, and 2D materials would readily degrade under a focused nA STEM probe [82]. In some cases, the use of multi-frame spectrum imaging with short dwell times may mitigate sample damage [83], and alternative approaches such as compressed-sensing or low-voltage (S)TEM should also be explored [84]. Finally, while the present method provides nanoscale spatial resolution, the method is not well suited for 2D spectral mapping across large areas, owing to the long acquisition time needed per pixel, as well as scan distortions related to the unconventional post-specimen optics. Alternative methods for high throughput SRO mapping should be considered.

4. Materials and methods

4.1. EXELFS acquisition

All electron microscopy and spectroscopy experiments were performed on a JEOL 2100F instrument with an accelerating voltage of 200 kV and a Schottky emitter. EELS was collected with a Gatan Imaging Filter (GIF) Quantum equipped with a Gatan K2 IS camera operated in electron counting mode [33]. The GIF high SNR aperture (5 mm) was used for all experiments. The dispersion was nominally set to 0.5 eV/channel, but, after EXELFS calibration on the Ti and Ni reference samples, the dispersion for all edges was adjusted to 0.485 eV/channel post acquisition. A custom post-specimen lens configuration was used, with a collection semi-angle that varied from 73 mR at 5 keV energy loss to 56 mR at 10 keV energy loss (Supplementary Fig. 1). For each EELS measurement, the spectrometer was initially focused on the zero loss peak, and then the F_x was re-focused on the edge of interest [19]. For all EELS measurements, the microscope was operated in STEM mode with a convergence semi-angle of 16 mR. Multiple acquisitions of ~60 s were performed, and individual spectra were then aligned and summed. Prior to summation, individual EELS datasets were processed to remove ‘hot pixels’ (pixels with extremely large or negative values due to problems with the counting software). After summation, plural scattering was removed with a Fourier ratio deconvolution as implemented in Gatan Digital Micrograph v.3 (Supplementary Fig. 2). To avoid saturation during zero-loss peak measurements, we used a reduced current and a CCD camera. The collection semi-angle for these measurements was 60 mR at 0 keV energy loss.

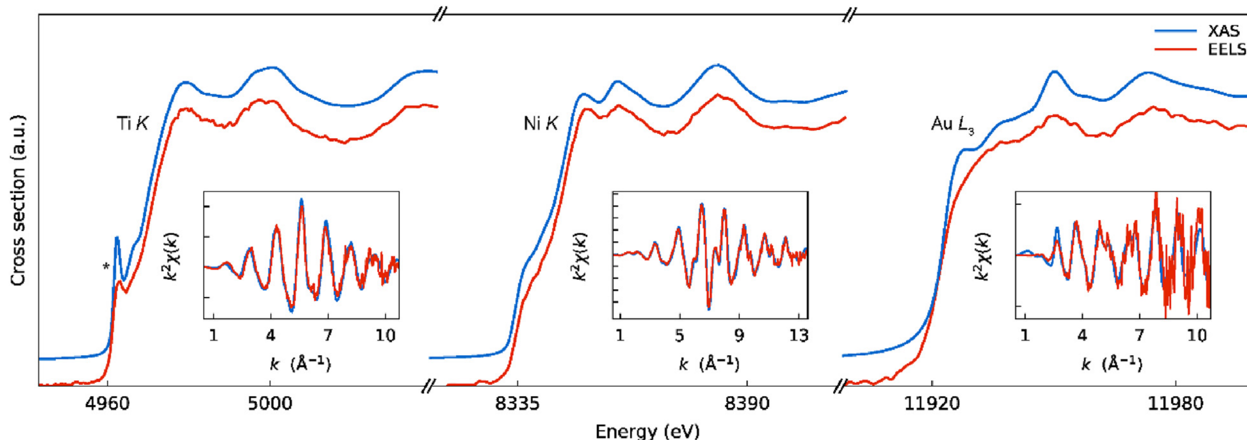

Fig. 2. Demonstration of high energy EELS and EXELFS. Normalized EELS and XAS comparison for the near edge structure region at the *K*-edge of Ti, the *K*-edge of Ni, and L_3-edge of Au. XAS data are shifted vertically for clarity. EELS calibration at high energy is poor, and slight energy shifts were required to align the EELS data with the XAS data. The * marks the Ti *K*-edge pre-peak. The insets show comparison between the corresponding EXELFS and EXAFS spectra; the *y*-axis tick marks are at every integer value.

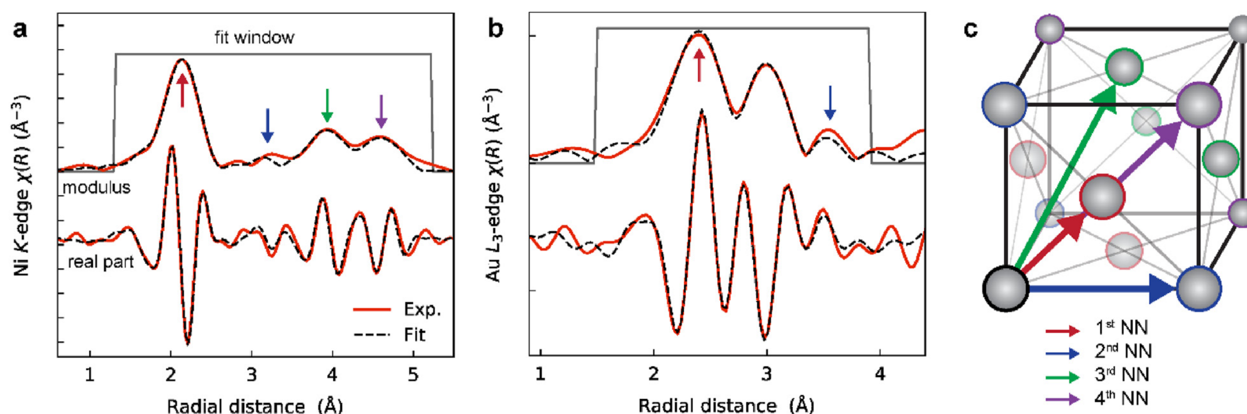

Fig. 3. Quantitative EXELFS processing. a Fit to the Ni *K*-edge data (uncorrected for electron phase shift), with an *R* window of 1.3–5.2 Å, and a *k* window of 2–13 Å^{-1}. b Fit to the Au L_3-edge data, with an *R* window of 1.5–3.9 Å, and a *k* window of 2–10 Å^{-1}. For both a and b, the *k*-space data was k^2-weighted prior to the Fourier transform, and the *y*-axis tick marks are at every integer value. Full fit parameters are given in Supplementary Tables 1 and 2. c FCC unit cell showing the 1st through 4th nearest neighbor (NN) bonds for the atom circled in black.

For the Ti *K*-edge measurement shown in Fig. 2, the beam current was 2 nA and the total acquisition time was 600 s, giving a total dose of 8×10^{12} electrons. The sample was a FIB lamella taken from bulk, polycrystalline Ti. The lamella had a thickness of $t/\lambda = 1.1$, where t is the sample thickness and λ is the inelastic mean free path. Using an estimated inelastic mean free path [85], the Ti sample was ~88 nm thick. For the Ni *K*-edge measurement shown in Fig. 2, the beam current was 6 nA and the total acquisition time was 1200 s, giving a total dose of 5×10^{13} electrons. The sample was prepared via FIB prep from a polycrystalline Ni source, and had a thickness of $t/\lambda = 1.1$ (~82 nm). For the Au L_3-edge measurement shown in Fig. 2, the beam current was 8 nA and the total acquisition time was 3000 s, giving a total dose of 2×10^{14} electrons. The sample was a sputtered polycrystalline Au film, and had a thickness of $t/\lambda = 1.2$ (~65 nm). Note that for this measurement, the STEM high tension was increased above 200 kV, since the spectrometer used here only allows for measurement of energy losses up to 10 keV. By increasing the high tension, the effective spectrometer energy loss is increased. For all of these experiments (meaning the spectra shown in Figs. 2 and 3), data was collected as the STEM probe continuously rastered across an area of several hundred nm^2 with a ~μs dwell time.

For the spatially resolved mapping of the Ni/BMG laminate shown in Fig. 4, the STEM-EXELFS spectrum image (SI) had a step size of 2 nm with a multi-frame SI acquisition of 30 passes and 0.01 s per pass, resulting in a total dwell time per pixel of 0.3 s per SI. Seven multi-frame SIs were acquired, aligned, and summed. The STEM probe current was 8 nA, and the spot size was ~3 nm. The average sample thickness across the SI area was $t/\lambda = 0.55$ (~39 nm). For each of the summed interfacial regions shown in Fig. 4, the local dose was 1×10^{13} electrons. The BMG sample was prepared as in Ref. [40], and a Ga^+ FIB was used to prepare the TEM specimen, with final thinning at 5 kV.

4.2. EXAFS acquisition

For Ni *K*-edge, Ti *K*-edge, and Au L_3-edge spectra of foils, all the data were taken from the web depository of synchrotron catalysis consortium at BNL at http://you.synchrotron.edu/scc2.

4.3. EXELFS and EXAFS data processing

EELS and XAS data were normalized using the Athena software package [44]. Low order polynomials were fit to the pre- and post-edge regions, allowing extraction of the normalized cross-section (Supplementary Fig. 2). The same normalization and background removal protocols were used for EELS and XAS data. The absolute

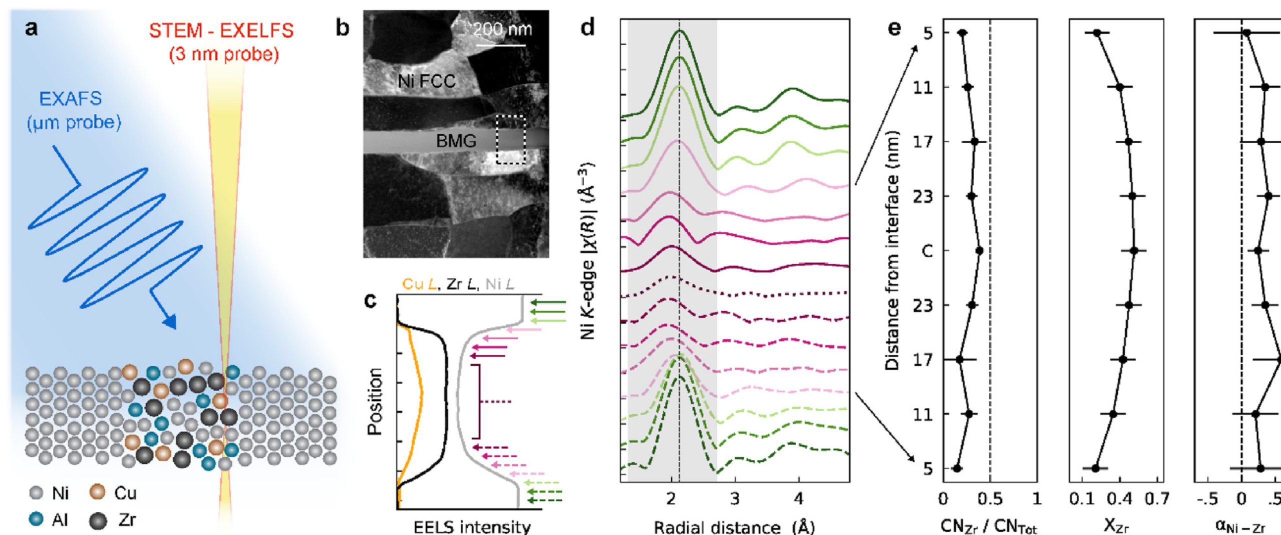

Fig. 4. Application of STEM-EXELFS to a crystalline/amorphous nanolaminate. a Schematic showing the Ni/BMG laminate structure in cross-section and the improved spatial resolution of STEM-EXELFS relative to synchrotron EXAFS. b STEM-ADF image of the laminate. The dashed box indicates the region of EELS analysis. c Raw EELS intensity data (arbitrary units) for the Cu *L*-edge, Zr *L*-edge, and Ni *L*-edge across the BMG layer. Data have been shifted along the intensity axis for clarity. Tick marks on the *y*-axis mark every 20 nm. The colored arrows mark the positions of EXELFS spectra shown in d. The spacing between the arrows is 6 nm. d Comparison of the Ni *K*-edge EXELFS $|\chi(R)|$ (k^2-weighted) at various locations within the sample. The spectra are color-coded with the arrows in c. Data are offset vertically for clarity, and the *y*-axis tick marks are at every integer value. Green spectra are from the Ni matrix, and purple spectra are from the BMG. The vertical dashed line is a guide for the eye. The grey box shows the *R*-space window for EXELFS fitting, and the *k*-space fitting window was 2–10 $Å^{-1}$. e Spatial dependence of the relative Ni CNs (left), the local Zr atom fraction (center), and the computed Warren-Cowley SRO parameter, α (right). On the *y*-axis, the 'C' indicates the central region of the BMG.

energy calibration for EELS at high energy is poor, so all EELS edges were aligned to the XAS data. Fitting the EXELFS data was performed using the Artemis software package [44], and details for each fit are given in the Supplementary Information.

Credit author statement

James L. Hart: Conceptualization, Methodology, Formal analysis, Investigation, Writing – Original draft. **Andrew C. Lang**: Conceptualization, Methodology, Investigation, Writing – review & editing. **Yuanyuan Li:** Methodology, Formal analysis, Investigation. **Sina Shahrezaei:** Resources. **Darius D. Alix-Williams:** Resources, Formal analysis. **Michael L. Falk:** Resources, Formal analysis, Writing – review & editing. **Suveen N. Mathaudhu:** Resources, Writing – review & editing. **Anatoly I. Frenkel:** Methodology, Formal Analysis, Writing – review & editing, Supervision. **Mitra L. Taheri:** Conceptualization, Methodology, Writing – Original draft, Supervision, Project administration, Funding acquisition.

Declaration of competing interest

The authors declare that they have no known competing financial interests or personal relationships that could have appeared to influence the work reported in this paper.

Data availability

Data will be made available on request.

Acknowledgments

The authors thank Ian MacLaren and Rebecca Cummings for helpful discussions regarding high energy EELS acquisition and processing; Simon Billinge for providing critical feedback on the BMG EXELFS fit; Kanit Hantanasirisakul for reviewing the manuscript; and James Nathaniel for providing the Au sample. The authors thank the Drexel Centralized Research Facilities for supporting electron spectroscopy measurements. JL Hart, AC Lang, and ML Taheri acknowledge funding in part from the National Science Foundation (NSF) MRI award #DMR-1429661, the US Department of Energy, Office of Basic Energy Sciences through contract DE-SC0020314, and the Office of Naval Research through contract N00014-20-1-2368. EXAFS analysis and modeling by AI Frenkel were supported as part of the Integrated Mesoscale Architectures for Sustainable Catalysis (IMASC), an Energy Frontier Research Center funded by the U.S. Department of Energy, Office of Science, Basic Energy Sciences under Award #DE-SC0012573. SN Mathaudhu and S Shahrezaei acknowledge the support of NSF CMMI award #1550986 and #1554632. ML Falk acknowledges funding from the National Science Foundation (NSF) under award #DMR- 1910066/1909733. This research used beam line 7-BM (QAS) of the National Synchrotron Light Source II, a U.S. DOE Office of Science User Facility operated for the DOE Office of Science by Brookhaven National Laboratory under contract no. DE-SC0012704. Beam line operations were supported in part by the Synchrotron Catalysis Consortium (U.S. DOE, Office of Basic Energy Sciences, grant no. DE-SC0012335).

Appendix A. Supplementary data

Supplementary data to this article can be found online at https://doi.org/10.1016/j.mtnano.2022.100298.

References

[1] D. Alloyeau, C. Ricolleau, C. Mottet, T. Oikawa, C. Langlois, Y. Le Bouar, N. Braidy, A. Loiseau, Nat. Mater. 8 (2009) 940–946.
[2] S. Alayoglu, P. Zavalij, B. Eichhorn, Q. Wang, A.I. Frenkel, P. Chupas, ACS Nano 3 (2009) 3127–3137.
[3] J. Pan, Y.P. Ivanov, W.H. Zhou, Y. Li, A.L. Greer, Nature 578 (2020) 559–562.
[4] Y.Q. Cheng, E. Ma, Prog. Mater. Sci. 56 (2011) 379–473.
[5] T.C. Pekin, J. Ding, C. Gammer, B. Ozdol, C. Ophus, M. Asta, R.O. Ritchie, A.M. Minor, Nat. Commun. 10 (2019) 2445.

[6] Y. Xie, D.M. Artymowicz, P.P. Lopes, A. Aiello, D. Wang, J.L. Hart, E. Anber, M.L. Taheri, H. Zhuang, R.C. Newman, K. Sieradzki, Nat. Mater. 20 (2021) 789–793.
[7] R. Zhang, S. Zhao, J. Ding, Y. Chong, T. Jia, C. Ophus, M. Asta, R.O. Ritchie, A.M. Minor, Nature 581 (2020) 283–287.
[8] Q. Ding, Y. Zhang, X. Chen, X. Fu, D. Chen, S. Chen, L. Gu, F. Wei, H. Bei, Y. Gao, M. Wen, J. Li, Z. Zhang, T. Zhu, R.O. Ritchie, Q. Yu, Nature 574 (2019) 223–229.
[9] B. Yin, S. Yoshida, N. Tsuji, W.A. Curtin, Nat. Commun. 11 (2020) 2507.
[10] F.X. Zhang, S. Zhao, K. Jin, H. Xue, G. Velisa, H. Bei, R. Huang, J.Y.P. Ko, D.C. Pagan, J.C. Neuefeind, W.J. Weber, Y. Zhang, Phys. Rev. Lett. 205501 (2017) 1–6.
[11] Y. Bu, Y. Wu, Z. Lei, X. Yuan, H. Wu, X. Feng, J. Liu, J. Ding, Y. Lu, H. Wang, Z. Lu, W. Yang, Mater. Today 46 (2021) 28–34.
[12] M.J. Krogstad, P.M. Gehring, S. Rosenkranz, R. Osborn, F. Ye, Y. Liu, J.P.C. Ruff, W. Chen, J.M. Wozniak, H. Luo, O. Chmaissem, Z.-G. Ye, D. Phelan, Nat. Mater. 17 (2018) 718–724.
[13] K. Konstantinou, F.C. Mocanu, T. Lee, S.R. Elliott, Nat. Commun. 10 (2019) 3065.
[14] P. Lee, P.H. Citrin, P. Eisenberger, B.M. Kincaid, Rev. Mod. Phys. 53 (1981) 769–806.
[15] A.I. Frenkel, Chem. Soc. Rev. 41 (2012) 8163–8178.
[16] L.M. Brown, Electron Microsc. Anal. Gr. Conf. (1997) 17–22.
[17] G. Blanche, G. Hug, M. Jaouen, A.M. Flank, Ultramicroscopy 50 (1993) 141–145.
[18] A.J. Craven, H. Sawada, S. Mcfadzean, I. Maclaren, Ultramicroscopy 180 (2017) 66–80.
[19] I. Maclaren, K.J. Annand, C. Black, A.J. Craven, Microscopy 67 (2018) 78–85.
[20] I. MacLaren, R.B. Cummings, F. Gordon, E. Frutos-Myro, S. McFadzean, A.P. Brown, A.J. Craven, Adv. Imag. Electron. Phys. (2019) 299–355.
[21] K.J. Annand, I. Maclaren, M. Gass, J. Nucl. Mater. 465 (2015) 390–399.
[22] R.F. Egerton, F. Wang, M. Malac, M.S. Moreno, F. Hofer, Micron 39 (2008) 642–647.
[23] D. Bach, R. Schneider, D. Gerthsen, J. Verbeeck, W. Sigle, Microsc. Microanal. 15 (2009) 505–523.
[24] A. Bendeddouche, R. Berjoan, E. Bêche, T. Merle-Mejean, S. Schamm, V. Serin, G. Taillades, A. Pradel, R. Hillel, J. Appl. Phys. 81 (1997) 6147–6154.
[25] Z.W. Yuan, S. Csillag, M.A. Tafreshi, C. Colliex, Ultramicroscopy 59 (1995) 149–157.
[26] M. Qian, M. Sarikaya, E.A. Stern, Ultramicroscopy 59 (1995) 137–147.
[27] S. Abaidia, V. Serin, G. Zanchi, Y. Kihn, J. Sévely, Philos. Mag. A 72 (1995) 1657–1670.
[28] F.M. Alamgir, H. Jain, D.B. Williams, R.B. Schwarz, Micron 34 (2003) 433–439.
[29] Y. Ito, F.M. Alamgir, H. Jain, D.B. Williams, R.B. Schwarz, Bulk Met, Glas., Boston, MA, 1999.
[30] P.E. Batson, A.J. Craven, Phys. Rev. Lett. 42 (1979) 893–897.
[31] P. Lu, P. Kotula, Microsc. Microanal. 17 (2011) 826–827.
[32] P. Nandi, E. Hoglund, X. Sang, R.R. Unocic, J.M. Howe, Microsc. Microanal. 23 (2017) 414–415.
[33] J.L. Hart, A.C. Lang, A.C. Leff, P. Longo, C. Trevor, R.D. Twesten, M.L. Taheri, Sci. Rep. 7 (2017) 8243.
[34] B.H. Goodge, D.J. Baek, L.F. Kourkoutis, ArXiv Prepr (2020). ArXiv2007.09747.
[35] K.A. DeRocher, P.J.M. Smeets, B.H. Goodge, M.J. Zachman, P.V. Balachandran, L. Stegbauer, M.J. Cohen, L.M. Gordon, J.M. Rondinelli, L.F. Kourkoutis, D. Joester, Nature 583 (2020) 66–71.
[36] D.H. Howe, J.L. Hart, R.M. Mcdaniel, M.L. Taheri, A.J.D. Magenau, ACS Macro Lett. 7 (2018) 1503–1508.
[37] V. Natu, J.L. Hart, M. Sokol, H. Chiang, M.L. Taheri, M.W. Barsoum, Angew. Chem. 131 (2019) 12785–12790.
[38] J.L. Hart, K. Hantanasirisakul, A.C. Lang, B. Anasori, D. Pinto, Y. Pivak, J.T. Van Omme, S.J. May, Y. Gogotsi, M.L. Taheri, Nat. Commun. 10 (2019) 522.
[39] I. MacLaren, T.A. Macgregor, C.S. Allen, A.I. Kirkland, Apl. Mater. 8 (2020), 110901.
[40] S. Shahrezaei, D.C. Hofmann, S.N. Mathaudhu, J. Mater. 71 (2019) 585–592.
[41] R.F. Egerton, R.A. Mcleod, M. Malac, Microsc. Res. Tech. 77 (2014) 773–778.
[42] M. Diociaiuti, L. Lozzi, M. Passacantando, S. Santucci, P. Picozzi, M. De Crescenzi, J. Electron. Spectrosc. Relat. Phenom. 82 (1996) 1–12.
[43] D.C. Koningsberger, R. Prins (Eds.), X-Ray Absorption: Principles, Applications, Techniques of EXAFS, SEXAFS, and XANES, John Wiley & Sons, New York, NY, 1988.
[44] B. Ravel, M. Newville, J. Synchrotron Radiat. 12 (2005) 537–541.
[45] J. Kim, D. Jang, J.R. Greer, Adv. Funct. Mater. 21 (2011) 4550–4554.
[46] M.Y. Tong, C.K.C. Lieou, I.J. Beyerlein, Phys. Rev. Mater. 3 (2019) 1–12.
[47] S.V. Ketov, Y.P. Ivanov, D. Şopu, D.V. Louzguine-Luzgin, C. Suryanarayana, A.O. Rodin, T. Schöberl, A.L. Greer, J. Eckert, Mater. Today Adv. 1 (2019) 1–9.
[48] C. Brandl, T.C. Germann, A. Misra, Acta Mater. 61 (2013) 3600–3611.
[49] W. Guo, J. Yao, E.A. Jägle, P.P. Choi, M. Herbig, J.M. Schneider, D. Raabe, Mater. Sci. Eng., A 628 (2015) 269–280.
[50] S. Ohsaki, S. Kato, N. Tsuji, T. Ohkubo, K. Hono, Acta Mater. 55 (2007) 2885–2895.
[51] Y.F. Sun, Y. Todaka, M. Umemoto, N. Tsuji, J. Mater. Sci. 43 (2008) 7457–7464.
[52] X. Wang, Q.P. Cao, Y.M. Chen, K. Hono, C. Zhong, Q.K. Jiang, X.P. Nie, L.Y. Chen, X.D. Wang, J.Z. Jiang, Acta Mater. 59 (2011) 1037–1047.
[53] S. Hilke, H. Rösner, D. Geissler, A. Gebert, M. Peterlechner, G. Wilde, Acta Mater. 171 (2019) 275–281.
[54] L. Tian, C.A. Volkert, Metals 8 (2018) 1–14.
[55] P. Zhang, J.J. Maldonis, M.F. Besser, M.J. Kramer, P.M. Voyles, Acta Mater. 109 (2016) 103–114.
[56] A.I. Frenkel, C.W. Hills, R.G. Nuzzo, J. Phys. Chem. B 105 (2001) 12689–12703.
[57] D.B. Miracle, Nat. Mater. 3 (2004) 697–702.
[58] J.M. Cowley, Phys. Rev. 77 (1950) 669–675.
[59] N. Norman, B.E. Warren, J. Appl. Phys. 22 (1951) 483–486.
[60] M. Matsuura, M. Sakurai, W. Zhang, A. Inoue, Mater. Sci. Forum (2007) 539–543, 1959–1963.
[61] X.J. Liu, X.D. Hui, G.L. Chen, T. Liu, Phys. Lett. 373 (2009) 2488–2493.
[62] A.I. Frenkel, A V Kolobov, I.K. Robinson, J.O. Cross, C.E. Bouldin, Phys. Rev. Lett. 89 (2002), 285503.
[63] G.S. Cargill, F. Spaepen, J. Non-Cryst. Solids 43 (1981) 91–97.
[64] C. Dong, Z.J. Wang, S. Zhang, Y.M. Wang, Int. Mater. Rev. 6608 (2019) 1743–2804.
[65] D. Ma, A.D. Stoica, L. Yang, X.L. Wang, Z.P. Lu, J. Neuefeind, M.J. Kramer, J.W. Richardson, T. Proffen, Appl. Phys. Lett. 90 (2007) 13–16.
[66] D.D. Alix-Williams, M.L. Falk, Phys. Rev. E 98 (2018) 1–11.
[67] D.B. Miracle, D.V. Louzguine-Luzgin, L.V. Louzguina-Luzgina, A. Inoue, Int. Mater. Rev. 55 (2010) 218–256.
[68] A.A. Deshmukh, A.A. Khond, J.G. Bhatt, U.A. Palikundwar, Phys. B Condens. Matter 630 (2022).
[69] K. Saksl, P. Jóvári, H. Franz, Q.S. Zeng, J.F. Liu, J.Z. Jiang, J. Phys. Condens. Matter 18 (2006) 7579–7592.
[70] A. Yevick, A.I. Frenkel, Phys. Rev. B 81 (2010), 115451.
[71] S.K. Gill, J. Huang, J. Mausz, R. Gakhar, S. Roy, F. Vila, M. Topsakal, W.C. Phillips, B. Layne, S. Mahurin, P. Halstenberg, S. Dai, J.F. Wishart, V.S. Bryantsev, A.I. Frenkel, J. Phys. Chem. B 124 (2020) 1253–1258.
[72] P.A. O'Day, J.J. Rehr, S.I. Zabinsky, G.E.J. Brown, J. Am. Chem. Soc. 116 (1994) 2938–2949.
[73] X. Hui, D.Y. Lin, X.H. Chen, W.Y. Wang, Y. Wang, S.L. Shang, Z.K. Liu, Scripta Mater. 68 (2013) 257–260.
[74] M. Sadeghilaridjani, Y.C. Yang, V. Hasannaeimi, C. Mahajan, S. Jha, M. Pole, Z. Xia, S. Mukherjee, ACS Appl. Mater. Interfaces 13 (2021) 9260–9271.
[75] F. Zhu, A. Hirata, P. Liu, S. Song, Y. Tian, J. Han, T. Fujita, M. Chen, Phys. Rev. Lett. 119 (2017), 215501.
[76] F. Walsh, M. Asta, R.O. Ritchie, Proc. Natl. Acad. Sci. USA 118 (2021), e2020540118.
[77] E. Antillon, C. Woodward, S.I. Rao, B. Akdim, T.A. Parthasarathy, Acta Mater. 190 (2020) 29–42.
[78] B. Chen, S. Li, H. Zong, X. Ding, J. Sun, E. Ma, Proc. Natl. Acad. Sci. USA 117 (2020) 16199–16206.
[79] Q. Li, H. Sheng, E. Ma, Nat. Commun. 10 (2019) 3563.
[80] J.L. Hart, K. Hantanasirisakul, A.C. Lang, Y. Li, F. Mehmood, R. Pachter, A.I. Frenkel, Y. Gogotsi, M.L. Taheri, Adv. Mater. Interfac. 8 (2021), 2001789.
[81] L. Tian, Z.W. Shan, E. Ma, Acta Mater. 61 (2013) 4823–4830.
[82] R.F. Egerton, P. Li, M. Malac, Micron 35 (2004) 399–409.
[83] L. Jones, A. Varambhia, R. Beanland, D. Kepaptsoglou, I. Griffiths, A. Ishizuka, F. Azough, R. Freer, K. Ishizuka, D. Cherns, Q.M. Ramasse, S. Lozano-Perez, P.D. Nellist, Microscopy 67 (2018) i98–i113.
[84] E. Monier, T. Oberlin, N. Brun, X. Li, M. Tencé, N. Dobigeon, Ultramicroscopy 215 (2020), 112993.
[85] D.R.G. Mitchell, J. Microsc. 224 (2006) 187–196.